Fine-scale segmentation of the crustal magma reservoir beneath the East Pacific Rise

Suzanne M. Carbotte[1]*, Milena Marjanović[1], Helene Carton[1], John C. Mutter[1], Juan Pablo Canales[2], Mladen R. Nedimović[1,3], Shuoshuo Han[1] and Michael R. Perfit[4]

The global mid-ocean ridge is segmented in its seafloor morphology and magmatic systems, but the origin of and relationships between this tectonic and magmatic segmentation are poorly understood[1-5]. At fast-spreading ridges, tectonic segmentation is observed on a fine scale[2,4,6-8], but it is unclear whether this partitioning also occurs in the magmatic system. Fine-scale tectonic segmentation could have a deep origin, arising from the distribution of upwelling mantle melt, or a shallow origin, linked to offset intruding dikes from long, more continuous crustal reservoirs[2,9]. Here we use seismic reflection data from the fast-spreading East Pacific Rise, between 8° 20′ N and 10° 10′ N, which includes a unique area where two documented volcanic eruptions have occurred[10-15], to image the crustal magma bodies in high resolution. We find that the magma reservoirs form 5- to 15-km-long segments that coincide with the fine-scale tectonic segmentation at the seafloor and that three lens segments fed the recent eruptions. Transitions in composition, volume and morphology of erupted lavas coincide with disruptions in the lens that define magmatic segments. We conclude that eruptions at the East Pacific Rise are associated with the vertical ascent of magma from lenses that are mostly physically isolated, leading to the eruption of distinct lavas at the surface that coincide with fine-scale tectonic segmentation.

Most volcanic and hydrothermal activity along the fast-spreading northern East Pacific Rise (EPR) occurs within a small (<20 m high, <500 m wide) depression known as the axial summit trough (AST) or along axis-centred ridges of pillow lavas[6-8,16]. These seafloor structures encompass the zone of primary eruptive fissures for the eruptions and dyke intrusions that build the upper crust and are readily identified in high-resolution sonar data from the EPR axis[2,4,6-8,16] (Fig. 1). The magma source reservoir for these volcanic events is a thin (tens of metres) lens of fully to partially molten magma, located in the mid-to-upper crust and roughly centred beneath, but wider (0.5–4 km) than the seafloor eruptive fissure zone above (for example, ref. 17). Seismic tomography data indicate that this thin magma lens is located above a broader, 4–6-km-wide, region extending into the lower crust that is thought to be composed of a crystal mush of hot rock and distributed melt[9].

New multi-channel seismic (MCS) reflection data are used here to characterize the present-day magma lens beneath a zone of modern volcanic eruptions at ∼9° 50′ N and adjoining EPR from 8° 20 to 10° 10′ N (Methods). From a series of lines shot along the ridge axis, the seismic line closest to the innermost axial zone (centre of the AST or axial pillow ridge) is identified (Fig. 1 and Supplementary Figs S1 and S2) and a composite profile

is constructed (Fig. 2). The composite profile provides a cross-sectional view of the magma lens at the location where modern hydrothermal venting, historic eruptions and eruptive fissures are narrowly focused. The seismic data reveal an axial magma lens (AML) reflection beneath ∼85% of the innermost axial zone that varies in depth over short spatial scales about an average depth of ∼1.6 km. However, the AML reflection is not a continuous event. Numerous disruptions in the AML are evident (Fig. 1b), including breaks with steps in AML two-way travel time (TWTT), edge diffractions in stack sections, or regions of two AML reflections that overlap in depth. Five of these discontinuities are resolved in MCS data acquired for three-dimensional (3D) imaging from ∼9° 37′ to 40′ N and 9° 42′ to 57′ N and correspond with offset and overlapping melt zones in plan view[18] (Supplementary Fig. S2a). Using the nature of lens discontinuities interpreted from the 3D volumes as a guide, minima criteria are defined (Methods) and AML disruptions are identified along the full length of the profile (Fig. 2). AML disruption zones, with lateral along-axis extents of up to 1.5 km, define a magma lens that is partitioned into segments 5–15 km long. AML depth varies within individual lens segments and many AML disruptions lie at local depth maxima (Fig. 2 and Supplementary Notes and Fig. S3).

Previously collected seismic reflection data from the region showed separate magma lens bodies beneath both limbs of the large overlapping spreading centre (OSC) at 9° 03′ N (ref. 19), as well as evidence for segmentation of the AML coincident with smaller offsets of the axis at 9° 37′ N and 9° 19–21′ N (ref. 17). These smaller offsets are classified as third-order tectonic discontinuities on the basis of offset length (0.5 and 1 km) and evidence for a ridge-flank trace indicating persistence for hundreds of thousands of years (refs 2–4). Our modern seismic data, acquired with a high-quality tuned seismic source and well located along the axial zone, indicate disruptions in the AML at both of these axial discontinuities as well as at all other identified third-order offsets (Fig. 2). Furthermore, the new data show that the smaller-scale or fourth-order offsets of the eruptive fissure zone[2,6] also coincide with segmentation of the underlying magma lens. These fourth-order discontinuities are defined by small lateral steps (50–500 m) in the AST or axial pillow ridges, or changes in width or trend of these structures[2,6,8]. All of these discontinuities are associated with small bends or steps in the broader (∼4 km wide) axial high and/or local pinches in the cross-axis morphology, indicating longevity for perhaps thousands of years[2,4,8], in spite of the small offset of the axial zone (Fig. 1 and Supplementary Figs S1 and S2). At most seafloor discontinuities (75%), a magma lens disruption zone is identified within the subsurface (within 1 km;
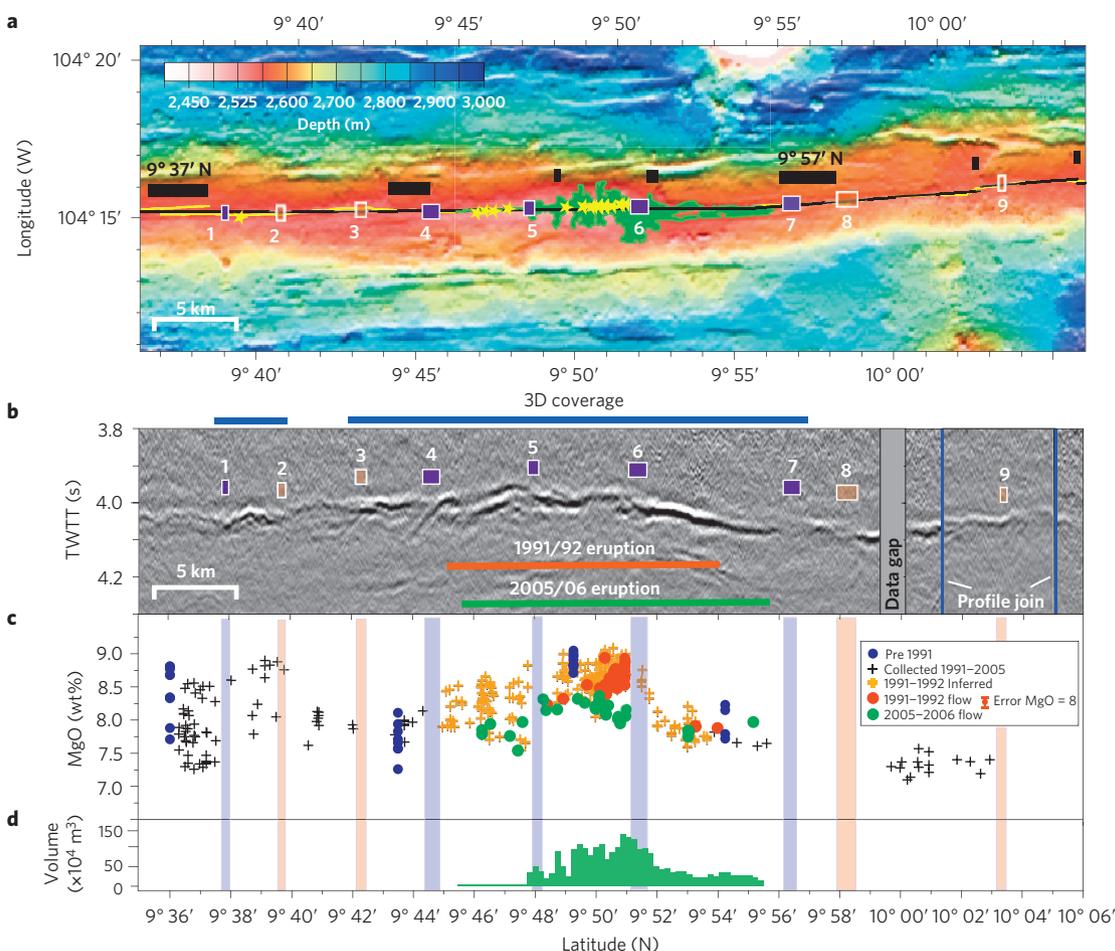
Figure 1 | Segmentation in seafloor structure, AML, lava geochemistry and eruption volume along the EPR 9° 35'–10° 06' N. a, Bathymetry showing location of axial eruptive zone (yellow line, from refs 8,12,16) and composite axial seismic profile (black). Black rectangles: third- (labelled) and fourth-order tectonic discontinuities. Yellow stars: hydrothermal vents[30]; green region: 2005–2006 lava flow[12]. **b**, Composite axial seismic reflection section (stacked) showing magma lens reflection and interpreted disruptions. TWTT, two-way travel time. Numbered rectangles in **a,b** indicate magma lens disruptions identified from seismic data (purple, data from 3D seismic volume). **c**, MgO composition of seafloor lavas located within 500 m of the axis (see Methods) colour-coded for eruption period. Microprobe analytic errors on natural glasses are ±1% of measured values and are indicated for MgO = 8.0 wt%. **d**, Volume of erupted 2005–2006 lavas[12] (Methods). Vertical bars (translucent purple and orange) mark magma lens disruptions from **a,b**.

Figs 1 and 2). From these relationships, we conclude that the fine-scale segmentation of the seafloor eruptive fissure zone is inherited from partitioning in the magma reservoir ~1.6 km below. Previous suggestions that fourth-order segmentation reflects shallow level processes associated with dyke intrusion from continuous magma reservoirs[1,2,6] can be ruled out.

Fine-scale segmentation in the chemistry of young seafloor lavas has long been recognized although the origin of this segmentation is not well understood[1]. A variety of factors may contribute to along-axis chemical diversity including magma evolution within crustal reservoirs, differences in mantle source composition and/or melt extraction within the mantle. These processes are expected to vary both spatially and temporally, but distinguishing among them is complicated by the limited age information available for seafloor lavas and the sparse sampling of most ridge areas. The EPR from ~9° N to the Clipperton transform fault is the most densely and frequently sampled portion of the global mid-ocean ridge. Major element compositions of axial lavas sampled in previous studies[1,3,13,14,20] (Methods) and known or assumed to have erupted in the past few hundred years reveal the presence of lavas of comparatively homogeneous composition separated by narrow regions of compositional transition/overlap (Fig. 1c). Regions of

mostly uniform lava composition coincide well with the magma lens segmentation mapped from the seismic data, with distinct lava chemistry above most lens segments. Where dense sampling spans magma lens discontinuities, compositional transitions and AML discontinuities are co-located within ≤1 km.

The two documented volcanic eruptions in this region occurred in 1991–1992 (ref. 10) and 2005–2006 (refs 11,12,15), and in roughly the same location with erupted lavas extending for 16–18 km along the ridge axis[10,12] (Fig. 1). Glass MgO concentrations, which are a proxy for lava temperatures, are highest above the 9° 48–9° 51.5' N magma lens segment, coincident with the central eruption source region for both eruptions[10,13]. Although the 2005–2006 lavas are slightly more evolved (lower MgO) than earlier lavas, spatial variations in lava geochemistry observed in the 1991–1992 lavas are preserved through the younger eruption (Fig. 1c and Supplementary Fig. S4) with more fractionated lavas erupted south of 9° 48' N and north of 9° 51.5' N (ref. 13). Geochemical data further indicate that northern lavas may have experienced shallower fractionation histories on average than lavas from the central region and for both eruptions, Zr/Y ratios are slightly elevated suggesting some differences in parental magmas[13]. We conclude that the three compositional zones erupted in both the
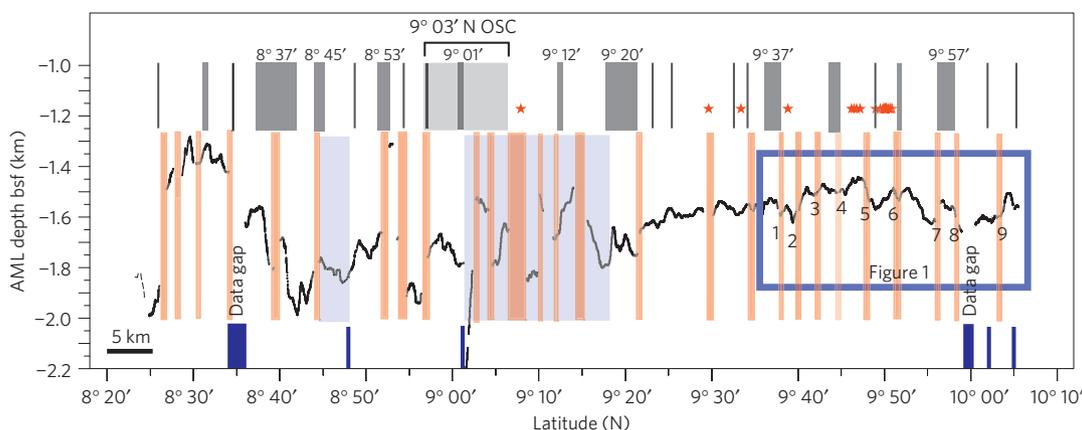
Figure 2 | Comparison of magma lens and bathymetric segmentation along the EPR 8° 20′–10° 10′ N. Depth below sea floor to AML reflection (black line) identified from seismic data (Methods and Supplementary Notes). Vertical orange bars indicate magma lens disruptions beneath the axis; the translucent purple shaded zones show areas where the seismic profile is >300 m from the axial zone, and/or the modern axis is difficult to identify and axial disruptions are poorly constrained. Grey lines/bars indicate bathymetric discontinuities (modified from ref. 8); 9° 03′ N OSC and third-order discontinuities are labelled. Short blue bars indicate data gaps and locations of joins between seismic lines of composite axial profile. Red stars indicate hydrothermal vents[30]. Bsf, below sea floor.

2005–2006 and earlier eruptions were fed from the three lens segments that underlie the present eruption zone. Furthermore, the preservation of compositional gradients through two eruptions, with more evolved compositions erupted in 2005–2006 relative to 1991–1992 and distinct parental melts inferred for northern lavas, indicates limited chemical mixing consistent with physical isolation of magma within adjacent lens segments.

Mapping of the 2005–2006 lava flow reveals three primary zones in lava morphology and erupted volume[12,21] with transitions also coincident with AML disruptions (Fig. 1d). Small eruptive volumes, entirely confined to the AST, are found above the southern lens segment. The largest eruptive volumes are mapped above the central segment where lavas extend to 2 km from the AST, with lower flow distances and mapped volumes above the northern segment. Differences in lava morphology have been attributed to variable lava effusion rates[21] and indicate different eruption conditions for the three lens segments.

These observations have significant implications for the mode of magma transport during dyke intrusion, a fundamental aspect of crustal formation about which little is known at fast-spreading ridges. Lateral magma transport at the EPR has been invoked to explain along-axis gradients in ridge properties including progressive deepening of the sea floor towards many ridge-axis discontinuities and the distinctive geometry of OSCs (for example, refs 2,4). Other indicators of lateral transport include magma flow markers and geochemical analyses of upper crustal exposures at Pito and Hess Deep, which require some component of horizontal magma transport in the dyke section[22,23]. However, our observations of distinct compositional and morphological segments in axial lavas from single eruptions coincident with segmentation of the underlying magma lens indicate that magma transport was predominantly vertical during these recent EPR eruptions (Fig. 3). Vertical magma transport has also been inferred along the southern EPR (ref. 24) where compositional boundaries in seafloor lavas of similar age are collocated with a discontinuity in the bathymetric axis at ∼17° 29′ S and a possible discontinuity in the underlying AML. If vertical magma ascent from the finely segmented magma reservoir inferred from our seismic data is the primary mode of magma transport at the EPR, an upper crust composed of small-scale accretionary units[2] is expected. Each unit will have distinct geochemical characteristics, physical dimensions and eruptive histories determined by the evolution of
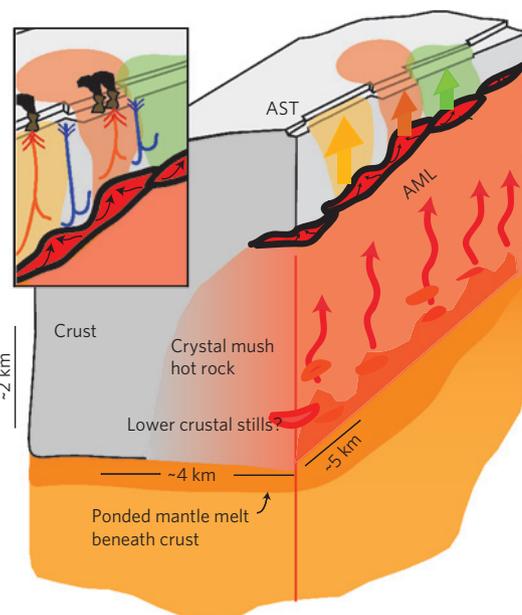

Figure 3 | Schematic representation of EPR magmatic system and 2005–2006 eruption. Segmented magma lens (red) sits atop zone of crystal mush (for example, ref. 9) and possible lower crustal sills[25] (light red). Mantle melts accumulate beneath crust[5,9] (orange). During dyking, compositionally distinct magmas intrude primarily vertically (broad arrows) from AML segments. Steps in AST coincide with AML segment boundaries. Possible factors contributing to AML segmentation include lower crustal melt focusing (red arrows), intrusions/eruptions and melt accumulation within the AML (black arrows), and (inset) variable cooling of AML through hydrothermal circulation. Inset: Arrows show hypothetical fluid downflow (blue) at seafloor discontinuities and upflow (red) beneath hydrothermal vents[29].

the chemical and physical properties of the underlying magma lens segment in response to ongoing magma replenishment and episodic withdrawal.

With magma present in the mid-crust beneath most of the ridge axis, why does it segregate into a series of 5–15 km elongate magma lens segments rather than form a continuous reservoir?

Both deep and shallow level processes are likely to contribute (Fig. 3). Focused melt transport may occur within the lower crust and shallow mantle through processes of melt channel formation or dyke intrusion from deep sills[25,26] forming punctuated sites of magma lens replenishment. Magma withdrawal associated with dyke intrusion and eruptions[27], and thermal erosion, stoping and crustal assimilation at the AML roof[28], are also likely to contribute to lens segmentation. Hydrothermal circulation above the magma lens may play an important role with local deepening and enhanced crystallinity within the AML predicted at sites of hydrothermal recharge[29]. The topography of the lens itself may play a key role in maintaining segmentation as buoyant melt migrates up-dip[19] and accumulates preferentially at local shoals. Our observations that many AML segments exhibit a convex shape in cross-section, and lens disruptions along the ridge axis often coincide with local depth maxima in the AML, are suggestive of this (Fig. 2 and Supplementary Notes).

Strong feedbacks are expected between hydrothermal cooling from above, dyke intrusion and eruption, and magma resupply from below[2,6]. These close linkages are evident in the relationships between hydrothermal vents, eruption history and AML structure within our study area. Most high-temperature vents in the region are located from 9° 46′ to 51′ N (refs 6,30) where both documented eruptions occurred. Here, the sea floor and AML shoal (Fig. 1 and Supplementary Fig. S3), and locally enhanced magma supply is inferred[2]. High-temperature vents form two clusters[6,30], centred above two of the three erupting lens segments and separated by a hydrothermal gap that spans the AML discontinuity and depth maxima at ∼9° 48′ N (Figs 1, 2). Differences in the chemistry and temporal evolution of vent fluids from these two clusters are documented[30] indicating distinct hydrothermal cells above the two lens segments, consistent with a closely coupled tectonic–magmatic–hydrothermal system.

Methods

Seismic reflection data acquisition and processing. Seismic reflection data were acquired during RV *Langseth* expedition MGL0812 and included 1–3 parallel lines shot along the EPR axis from 8° 20 to 10° 10′ N as well as a suite of lines shot perpendicular to the ridge for 3D imaging (Supplementary Fig. S1). Two 3,300-cubic-inch broadband source arrays were used in flip-flop mode with a 37.5 m shot interval. Data were recorded on four 6-km-long, 468-channel streamers with a 12.5 m receiver group spacing and a sampling interval of 2 ms. The recorded signal has a bandwidth ranging from ∼2 to 100 Hz with a dominant frequency of 10–30 Hz.

Reflection data used here were processed assuming a 2D geometry using recorded signals from one streamer and combining shots from both air-gun arrays providing a common midpoint fold of 78 and common midpoint spacing of 6.25 m. The pre-stack processing sequence includes merge of shot and navigation data, geometry definition, band-pass filter (2–7–100–125 Hz), trace edit, amplitude correction for spherical divergence and $f-k$ filter, surface-consistent amplitude correction, velocity analysis and normal move-out correction. The data are stacked for AML and sea floor using all traces to source–receiver offsets of 3 km and for the layer 2A horizon using traces from 1,500 to 3,000 m. The post-stack processing sequence includes sea floor and primary multiple mute to reduce migration noise, Kirchhoff time migration, and merge of layer 2A and AML sections. All processing is conducted using Paradigm's processing suite Focus.

From migrated sections, TWTTs to the AML reflection and the seismic layer 2A horizon are digitized using a guided digitizer tool and smoothed with a median filter (Supplementary Fig. S3). Estimated picking errors for all events are ±0.008 s. Seismic horizons are converted to depth assuming constant velocities of 2.26 km s⁻¹ for layer 2A and 5.5 km s⁻¹ for layer 2B. Stacking errors of ±0.016 s for layer 2A and ±0.008 s for the AML/seafloor events are estimated from the range of constant velocity stacks that optimally stack each event. Combined stacking and picking errors are ±0.018 s for the base of layer 2A and ±0.011 s for the AML, equivalent to depth uncertainties of ±20 m and ±35 m respectively for these events. See Supplementary Notes for further discussion of limitations in interpretation of AML structure from the 2D sections.

Identification of magma lens discontinuities. Within the region of 3D MCS coverage, disruptions in the axis-centred image of the AML are interpreted using the 3D data set and correspond with broad zones of overlapping and offset melt lenses (Supplementary Figs S1 and S2). Beyond this area, discontinuities in the

AML event are identified where at minimum two of the following criteria are met: break in AML continuity with abrupt step in TWTT of >30 ms; gap in AML event of >400 m; edge diffraction in the stacked section indicating abrupt change in physical properties; abrupt change in AML amplitude; presence of 2 AML events that overlap by >400 m. Further discussion of imaging limitations and uncertainties in interpretation of AML segmentation is included in Supplementary Notes.

Erupted volume of 2005/2006 lavas. Along-axis variations in volume of the 2005–2006 lavas are calculated within 300 m bins oriented perpendicular to the axis using the mapped area of the lava flow from ref. 12 and assuming a uniform 1.5 m flow thickness.

Data sources. MCS data used in this study are available through the Marine Geoscience Data System (http://www.marine-geo.org/tools/search/entry.php?id=MGL0812). Bathymetric data are from the GMRT Synthesis (http://www.marine-geo.org/tools/maps_grids.php). Hydrothermal vent locations are from the Ridge2000 Data Portal (http://www.marine-geo.org/portals/ridge2000/vents.php?feature_id=EPR).

Geochemical data are from refs 1,3,13,14,20 (available from PetDB, www.petdb.org) and the 'Basalt Glasses from the EPR' compilation of M. Perfit available through http://www.earthchem.org/library/search. See refs 3,13 for discussion of analytical methods. Samples are filtered for those located within ±500 m of the axis.

References

1. Langmuir, C. H., Bender, J. F. & Batiza, R. Petrological and tectonic segmentation of the East Pacific Rise, 5° 30′–14° 30′ N. *Nature* **322,** 422–429 (1986).
2. Macdonald, K. C. *et al.* A new view of the mid-ocean ridge from the behaviour of ridge-axis discontinuities. *Nature* **335,** 217–225 (1988).
3. Smith, M. C. *et al.* Magmatic processes and segmentation at a fast spreading mid-ocean ridge: Detailed investigation of an axial discontinuity on the East Pacific Rise crest at 9° 37′ N. *Geochem. Geophys. Geosyst.* **2,** 1040 (2001).
4. White, S. M. *et al.* Correlation between volcanic and tectonic segmentation of fast-spreading ridges: Evidence from volcanic structures and lava flow morphology on the East Pacific Rise at 9°–10° N. *J. Geophys. Res.* **107,** 2173 (2002).
5. Toomey, D. R., Jousselin, D., Dunn, R. A., Wilcock, W. S. D. & Detrick, R. S. Skew of mantle upwelling beneath the East Pacific Rise governs segmentation. *Nature* **446,** 409–414 (2007).
6. Haymon, R. M. *et al.* Hydrothermal vent distribution along the East Pacific Rise crest (9° 09′–9° 54′ N) and its relationship to magmatic and tectonic processes on fast spreading Mid-Ocean Ridges. *Earth Planet. Sci. Lett.* **104,** 513–534 (1991).
7. Fornari, D. J., Haymon, R. M., Perfit, M. R., Gregg, T. K. P. & Edwards, M. H. Axial summit trough of the East Pacific Rise 9°–10° N: Geological characteristics and evolution of the axial zone on fast spreading mid-ocean ridges. *J. Geophys. Res.* **103,** 9827–9855 (1998).
8. White, S. M., Haymon, R. M. & Carbotte, S. A new view of ridge segmentation and near-axis volcanism at the East Pacific Rise, 8°–12° N, from EM300 multibeam bathymetry. *Geochem. Geophys. Geosyst.* **7,** Q12O05 (2006).
9. Dunn, R. A., Toomey, D. R. & Solomon, S. C. Three-dimensional seismic structure and physical properties of the crust and shallow mantle beneath the East Pacific Rise at 9° 30′ N. *J. Geophys. Res.* **105,** 23537–23555 (2000).
10. Haymon, R. M. *et al.* Volcanic eruption of the mid-ocean ridge along the East Pacific Rise crest at 9° 45–52′ N: Direct submersible observations of seafloor phenomena associated with an eruption event in April, 1991. *Earth Planet. Sci. Lett.* **119,** 85–101 (1993).
11. Tolstoy, M. *et al.* A sea-floor spreading event captured by seismometers. *Science* **314,** 1920–1922 (2006).
12. Soule, S. A., Fornari, D. J., Perfit, M. R. & Rubin, K. H. New insights into mid-ocean ridge volcanic processes from the 2005–2006 eruption of the East Pacific Rise, 9° 46′ N–9° 56′ N. *Geology* **35,** 1079–1082 (2007).
13. Goss, A. R. *et al.* Geochemistry of lavas from the 2005–2006 eruption at the East Pacific Rise, 9° 46′ N–9° 56′ N: Implications for ridge crest plumbing and decadal changes in magma chamber compositions. *Geochem. Geophys. Geosyst.* **11,** Q05T09 (2010).
14. Perfit, M. *et al.* Lava geochemistry as a probe into crustal formation at the East Pacific Rise. *Oceanography* **25,** 21–24 (2012).
15. Rubin, K. H. *et al.* Volcanic eruptions in the deep sea. *Oceanography* **25,** 142–157 (2012).
16. Soule, S. A., Escartín, J. & Fornari, D. J. A record of eruption and intrusion at a fast spreading ridge axis: Axial summit trough of the East Pacific Rise 9–10° N. *Geochem. Geophys. Geosyst.* **10,** Q10T07 (2009).

17. Kent, G. M., Harding, A. J. & Orcutt, J. A. Distribution of magma beneath the East Pacific Rise between the Clipperton transform and the 9° 17′ N deval from forward modeling of common depth point data. *J. Geophys. Res.* **98,** 13945–13969 (1993).

18. Carton, H. D. *et al.* Three-dimensional seismic reflection images of axial melt lens and seismic layer 2A between 9° 42′ N and 9° 57′ N on the East Pacific Rise. *EOS Trans. AGU abstr.* OS21C-1514 (2010).

19. Kent, G. M. *et al.* Evidence from three-dimensional seismic reflectivity images for enhanced melt supply beneath mid-ocean ridge discontinuities. *Nature* **406,** 614–618 (2000).

20. Sims, K. W. W. *et al.* Aberrant youth: Chemical and isotopic constraints on the origin of off-axis lavas from the East Pacific Rise, 9°–10° N. *Geochem. Geophys. Geosyst.* **4,** 8621 (2003).

21. Fundis, A. T., Soule, S. A., Fornari, D. J. & Perfit, M. R. Paving the seafloor: Volcanic emplacement processes during the 2005–2006 eruptions at the fast spreading East Pacific Rise, 9° 50′ N. *Geochem. Geophys. Geosyst.* **11,** Q08024 (2010).

22. Varga, R. J., Horst, A. J., Gee, J. S. & Karson, J. A. Direct evidence from anisotropy of magnetic susceptibility for lateral melt migration at superfast spreading centers. *Geochem. Geophys. Geosyst.* **9,** Q08008 (2008).

23. Stewart, M. A., Karson, J. A. & Klein, E. M. Four-dimensional upper crustal construction at fast-spreading mid-ocean ridges: A perspective from an upper crustal cross-section at the Hess Deep Rift. *J. Volcanol. Geotherm. Res.* **144,** 287–309 (2005).

24. Bergmanis, E. C., Sinton, J. & Rubin, K. H. Recent eruptive history and magma reservoir dynamics on the southern East Pacific Rise at 17° 30′ S. *Geochem. Geophys. Geosyst.* **10,** Q12O06 (2007).

25. Kelemen, P. B., Koga, K. & Shimizu, N. Geochemistry of gabbro sills in the crust-mantle transition zone of the Oman ophiolite: Implications for the origin of the oceanic lower crust. *Earth Planet Sci. Lett.* **146,** 475–488 (1997).

26. Natland, J. H. & Dick, H. J. B. Paired melt lenses at the East Pacific Rise and the pattern of melt flow through the gabbroic layer at a fast-spreading ridge. *Lithos* **112,** 73–86 (2009).

27. Mutter, J. C. *et al.* Seismic images of active magma systems beneath the East Pacific Rise between 17° 05′ and 17° 35′ S. *Science* **21,** 391–395 (1995).

28. Coogan, L. A., Mitchell, N. C. & O'Hara, M. J. Roof assimilation at fast-spreading ridges: An investigation combining geophysical, geochemical and field evidence. *J. Geophys. Res.* **108,** 2002 (2003).

29. Fontaine, F. J., Olive, J-A., Cannat, M., Escartín, J. & Perol, T. Hydrothermally-induced melt lens cooling and segmentation along the axis of fast- and intermediate-spreading centers. *Geophys. Res. Lett.* **38,** L14307 (2011).

30. Von Damm, K. L. in *Mid-Ocean Ridges: Hydrothermal Interactions Between the Lithosphere and Ocean* (ed. German, C. R.) 285–304 (AGU Geophys. Mono., Vol. 148, American Geophysical Union, 2004).

Author contributions

All authors (except M.R.P. and S.H.) participated in the MCS field experiment. M.M. carried out the MCS data processing, S.M.C. and M.M. interpreted the data. M.R.P. contributed geochemical data and interpretation. S.M.C. wrote the paper with contributions from all co-authors.

Additional information

Supplementary information is available in the online version of the paper. Reprints and permissions information is available online at www.nature.com/reprints. Correspondence and requests for materials should be addressed to S.M.C.

Competing financial interests

The authors declare no competing financial interests.